Melt Viscosity, Elasticity, and Morphology of Reactively Compatibilized Polyamide 6/Styrene−Acrylonitrile Blends in Shear and Elongation

C. Sailer and U. A. Handge*

Institute of Polymers, Department of Materials, ETH Zurich, Wolfgang-Pauli-Strasse 10, 8093 Zurich, Switzerland

Received November 24, 2006; Revised Manuscript Received January 25, 2007

ABSTRACT: The melt rheology of reactively compatibilized polyamide 6/styrene−acrylonitrile (PA 6/SAN) blends was studied in linear viscoelastic shear oscillations, simple elongation to a large stretch ratio, and subsequent recovery. In addition, we examined and quantified the blend morphology and the flow-induced changes of the morphology. Three PA 6/SAN blends with different composition ratios of PA 6 and SAN (70/30, 50/50, 30/70) were prepared. Our experiments reveal that the asymmetric properties of the compatibilized interface strongly influence the rheological and morphological properties of the blends. The linear viscoelastic properties were discussed by applying the fractional Zener model. In particular, the data of the PA 6/SAN 30/70 blend indicate that an elastic network between neighboring PA 6 domains was formed. In simple elongation, the transient elongational viscosity of this blend exceeded the linear viscoelastic prediction of the fractional Zener model, whereas for the PA 6/SAN 70/30 blend the theoretical prediction of the elongational viscosity agreed well with the experimental data. The recovered stretch of all blends was much larger than the recovered stretch of pure PA 6 and SAN. This increase of elasticity was caused by the interfacial tension driven recovery and by the effects of reactive compatibilization. The morphological analysis showed that during elongation the phase domains of all blends were strongly stretched and retracted to an isotropic shape during recovery.

Introduction

Blending of polymers is an efficient method to develop new materials with specifically tailored end-use properties. Compatibilization of two-phase polymer blends is necessary in order to reduce the size of the phase domains, to stabilize the morphology against phase coarsening, and to enhance the interfacial adhesion between the two phases in the solid state.[1] A technologically highly important method is to form the compatibilizing agent by a chemical reaction in situ during melt mixing ("reactive compatibilization"). Thereby a third component that is miscible with one blend component and capable of reacting with reactive functional groups of the other component is added before melt blending. The chemical reaction generates graft or block copolymers at the interface and leads to compatibilization of the two phases.[2]

Currently, reactive compatibilization has become a state of the art technology that is applied for various commercial blends, e.g., blends of polyamide 6 (PA 6) and acrylonitrile−butadiene−styrene (ABS).[3−5] Accordingly, the reactive coupling of PA 6 and styrenic polymers by reactive agents that contain maleic anhydride has been investigated for more than two decades. Whereas the majority of these studies focused on the effect of reactive compatibilization on the morphology and the solid-state properties of these blends,[6−11] only a limited number of studies were devoted to their melt rheology, mainly to shear in the linear viscoelastic regime. The addition of a reactive compatibilizer to blends of PA 6 and styrenic polymers significantly increases the complex modulus.[12] The interfacial properties of reactively compatibilized blends with droplet−matrix morphologies were investigated by applying the emulsion model of Palierne.[13,14] In compatibilized polypropylene/polyamide 6 (PP/PA 6) blends the interfacial tension decreased with increasing concentration of maleic anhydride.[15] In addition to the form relaxation, another relaxation process, which was primarily observed for polystyrene/poly(methyl methacrylate) blends compatibilized by diblock copolymers,[16] was also found for PP/PA 6 blends with a high degree of compatibilization[15] and for reactively compatibilized polyethylene/polyamide 6 blends.[17] This additional relaxation process was related to an anisotropic interfacial tension which arises from gradients of the compatibilizer concentration on the surface of the compatibilized drops.[18,19] Recently, the effect of compatibilization on the recovery of immiscible blends after shear flow was investigated.[20,21] The addition of the compatibilizer increased the ultimate recovery of the blends and the time scale of recovery compared to uncompatibilized blends which was explained by flow-induced gradients of the compatibilizer concentration.

In compatibilized polymer blends gradients of compatibilizer on the drop surface strongly influence the deformation of single drops.[22,23] Numerical simulations[24−26] and experiments[27] showed that for large surface Péclet numbers drops deform more in the presence of a compatibilizer compared to the case of a constant interfacial tension. For low surface Péclet numbers a reduced droplet deformation is theoretically predicted[24−26] because of the dilution of the compatibilizer density on the surface of the stretched drop. A decrease of the stretch ratio was observed experimentally for compatibilized drops with a high viscosity ratio[27] and for drops with a high compatibilizer concentration.[28]

In this article, we investigate the rheological behavior of reactively compatibilized blends and focus on the viscous and elastic properties in linear viscoelastic oscillatory shear flow, in melt elongation to a large stretch ratio, and in subsequent recovery. In addition, the blend morphology and the morphological changes during flow are examined by atomic force microscopy and quantified. Previous studies have elucidated the

* Corresponding author. E-mail: ulrich.handge@mat.ethz.ch.

10.1021/ma062705c CCC: $37.00
Published on Web 02/23/2007

Table 1. Properties of the Blend Components

	T_g[b] (°C)	T_m[b] (°C)	M_n (g/mol)	M_w (g/mol)	M_w/M_n	ρ at 25 °C[c] (g/cm^3)	ρ at 240 °C[c] (g/cm^3)	η_0 at 240 °C (Pa s)
PA 6	53	221	23 000	121 000	5.3	1.145	0.984	8400
SAN[a]	109		57 800	150 000	2.6	1.082	0.989	2400

[a] The SAN grade includes 6.8 wt % SANMA. [b] Determined from second-heating-scan DSC thermograms (heating rate: 10 K/min). [c] Determined by the buoyancy method and *pVT* measurements.

Table 2. Composition of the PA 6/SAN Blends

blend	abbrev	φ_{PA6} (wt %)	φ_{SAN} (wt %)	φ_{SANMA} (wt %)
PA 6/SAN 70/30	PA70	70	28.0	2.0
PA 6/SAN 50/50	PA50	50	46.6	3.4
PA 6/SAN 30/70	PA30	30	65.2	4.8

linear and nonlinear rheology of noncompatibilized blends (see, e.g., refs 29−37). In this work, we study nondilute reactively compatibilized blends of PA 6 and styrene−acrylonitrile (SAN). Three different concentrations of PA 6 were chosen in order to prepare blends with disperse and cocontinuous morphologies. In contrast to PA 6/ABS blends in PA 6/SAN blends the SAN phase does not contain rubber particles which would mask the effects of reactive compatibilization on the rheological and morphological properties.

Experimental Section

Materials. The components of the blends were polyamide 6 (PA 6, Ultramid B4) and styrene−acrylonitrile copolymer (SAN) (BASF AG, Ludwigshafen am Rhein, Germany). Before blending 6.8 wt % of a styrene−acrylonitrile−maleic anhydride terpolymer (SAN-MA) was added to the SAN grade. The terpolymer was composed of 2 wt % maleic anhydride, 29 wt % acrylonitrile, and 69 wt % styrene, and the weight-average molecular weight was 115 000 g/mol. On average, one SANMA chain carried ∼20 maleic anhydride groups that are randomly distributed along the backbone of the terpolymer. SANMA is miscible with SAN and acts as reactive agent. The temperature of extrusion and rheological measurements was 240 °C. At this temperature the ratio of the zero shear rate viscosities of PA 6 to SAN was 3.5. Table 1 lists some characteristic properties of PA 6 and SAN.

Prior to melt blending, the pellets of the components were premixed and dried in vacuum at 80 °C for 7 days. The blends were prepared using a corotating twin-screw extruder (Brabender, Duisburg, Germany) at a temperature of 240 °C. The screw diameter was 25 mm, the *L*/*D* ratio was 22, and the number of screw rotations was set to 50 min^{-1}. During extrusion, the extruded strand was piled up to blobs of roughly equal mass (≈15 g). Then the blobs were compression-molded in vacuum at 240 °C to rectangular plates with dimensions 100 × 70 × 2 mm^3. The samples for rheological experiments were prepared by milling these plates into cylindrical samples with a diameter of 22 mm and a thickness of 2 mm for shear experiments and into rectangular samples of dimensions 56 × 7 × 2 mm^3 for elongational experiments. In order to prepare blends with different types of morphology, three different composition ratios were chosen. The weight fraction of PA 6 was 30% (abbreviated by PA30), 50% (PA50), and 70% (PA70). The absolute weight fractions φ_i of PA 6, SAN, and SANMA of the blends are listed in Table 2. Because of the constant SANMA content in SAN, the ratio of SANMA to PA 6 was different in each blend. The pure components were also extruded and compression-molded under the same conditions as the blends.

During melt mixing the maleic anhydride groups of SANMA are capable of reacting with the amino end groups of PA 6. The reaction occurs at the interface between the blend components and generates comblike SANMA-*graft*-PA 6 chains which leads to compatibilization of the phases (see Figure 1). The reaction proceeds very fast in the early stage of mixing, i.e., shortly after melting of the solid pellets of PA 6 and SAN.[38−40]

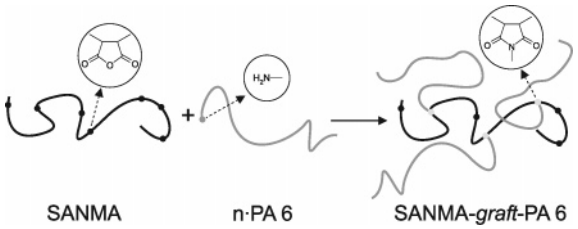

Figure 1. Schematic illustration of the compatibilizing reaction between SANMA and PA 6.

Rheology. Linear viscoelastic shear oscillations were performed using the shear rheometer UDS 200 (Physica, Stuttgart, Germany) at $T = 240$ °C in a nitrogen atmosphere. A parallel plate geometry was used with a plate diameter of 25 mm. The gap between the plates was set to 1.8 mm, and the shear amplitude was $\gamma_0 = 0.03$. Prior to the shear oscillations, time sweep experiments at constant frequency $\omega_0 = 0.1$ rad/s and shear amplitude $\gamma_0 = 0.03$ were conducted to check the thermal stability of the materials.

Melt elongation and subsequent recovery experiments were performed using the uniaxial elongational rheometer RME at $T = 240$ °C.[41] Two different Hencky strain rates were chosen, i.e., $\dot{\epsilon}_0 = 0.1$ s^{-1} and $\dot{\epsilon}_0 = 0.3$ s^{-1}. The maximum Hencky strain was $\epsilon_{max} = 1.8$, which corresponds to the stretch ratio $\lambda_{max} = \exp(\epsilon_{max}) = 6.0$. In order to perform recovery experiments, a pneumatically driven pair of scissors is installed in our RME (see refs 36 and 37 for details). After elongation to $\epsilon_{max} = 1.8$ at $\dot{\epsilon}_0 = 0.3$ s^{-1} the scissors cut the sample at one end so that the sample could recover freely.

Morphology. The morphology of (i) the extruded strand, (ii) undeformed, (iii) elongated, and (iv) recovered samples was examined by atomic force microscopy (AFM). The elongated samples were quenched in less than 1 s using a special quenching device which is described in ref 42. Cutoffs of the samples were prepared and glued into special holders for the AFM investigations. In order to obtain flat surfaces, the samples were microtomed parallel to the direction of stretching under cryo conditions at $T = -120$ °C with a diamond knife. The block phases were analyzed using the Nanoscope IIIa scanning probe microscope (Digital Instruments, Santa Barbara, CA). All images were collected in tapping mode using silicon cantilevers with natural frequencies in the 300 kHz range and force constants of about 42 N/m. During scanning the ratio of set-point amplitude A_{sp} to driving amplitude A_0 was 0.1 (hard tapping). These tuning parameters provide good stiffness related contrast of the phase images. The size of the scan area and the resolution of the AFM were adjusted to obtain an optimal balance between the resolution of the microstructure (e.g., micelles) and a large scanning area.

Results

Linear Viscoelastic Shear Oscillations. Figure 2 presents the complex modulus $G^* = G' + iG''$ of the pure components and the PA 6/SAN blends as a function of frequency ω at $T = 240$ °C. The storage and the loss modulus of PA 6 and SAN decrease with decreasing frequency and attain a shape that is typical for polydisperse homopolymers. At low frequencies, the pure components almost reach the terminal zone with $G' \propto \omega^2$ and $G'' \propto \omega$. On the contrary, the dynamic moduli of the blends display a more complex behavior. At large frequencies, G' and G'' of the blends vary monotonically with PA 6 concentration

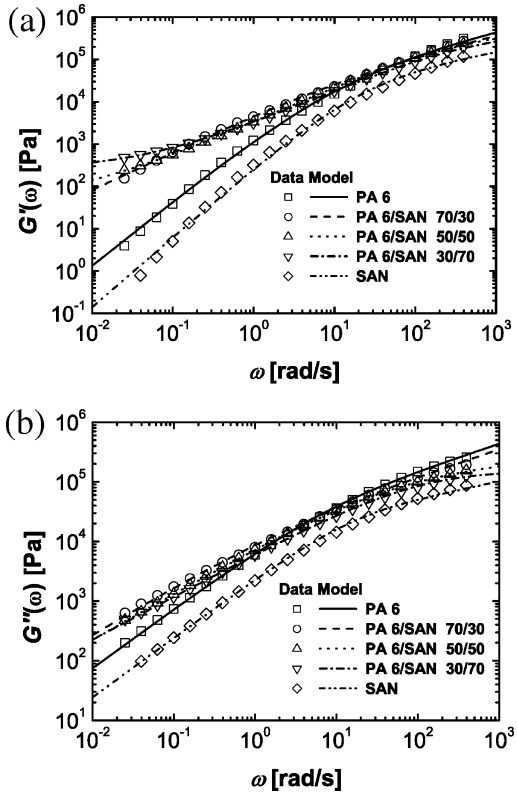

Figure 2. (a) Storage modulus G' and (b) loss modulus G'' as a function of frequency ω for PA 6 and SAN and the three different PA 6/SAN blends at $T = 240$ °C. The weight fractions of PA 6 and SAN are indicated. The solid lines are the results of a least-squares-fit of the fractional Zener model; see eqs 11 and 12.

between the values of the pure components. At low ω, the dynamic moduli of the blends exceed the values of the blend components. The shape of the log G' vs log ω curve of the PA30 and the PA50 blend is convex, which indicates that a ω-independent plateau possibly exists at very low frequencies. This tendency to form a low-frequency plateau in G' is much less pronounced for the PA70 blend. In contrast to the shape of log G' vs log ω, a power law behavior for G'' with exponents smaller than unity is observed for all PA 6/SAN blends at low ω.

Melt Elongation and Recovery. The transient elongational viscosity $\mu(t)$ is defined by

$$\mu(t) = \sigma(t)/\dot{\epsilon}_0 \tag{1}$$

where $\sigma(t)$ denotes the measured tensile stress. The transient elongational viscosity of the pure components and the PA 6/SAN blends at $T = 240$ °C for $\dot{\epsilon}_0 = 0.1$ s^{-1} and $\dot{\epsilon}_0 = 0.3$ s^{-1} is presented in Figure 3. The elongational viscosity of the pure components increases monotonically with time and attains a stationary value at large times (Figure 3a) which corresponds to the Trouton ratio 3. The elongational viscosity of the PA 6/SAN blends increases more rapidly than $\mu(t)$ of pure PA 6 and SAN and exceeds the viscosity of the components at larger times. In contrast to the pure components and the PA70 blend (Figure 3b), the $\mu(t)$ values for $\dot{\epsilon}_0 = 0.1$ s^{-1} and $\dot{\epsilon}_0 = 0.3$ s^{-1} of the PA50 blend and the PA30 blend differ at larger times (Figure 3c,d). This strain rate dependent behavior is mostly pronounced for the PA30 blend.

After elongation to $\epsilon_{max} = 1.8$ with Hencky strain rate $\dot{\epsilon}_0 = 0.3$ s^{-1} the scissors cut the sample, and the transient recovery of the blends was measured. The time-dependent recovered stretch λ_r is defined by

$$\lambda_r(t') = L_{max}/L(t') \tag{2}$$

where L_{max} denotes the length of the sample at cutting time $t = t_{max}$, and $L(t')$ is the length of the sample at recovery time $t' = t - t_{max}$.

Figure 4 presents the recovered stretch λ_r of the pure components and the PA 6/SAN blends as a function of recovery time t'. The recovered stretch of the blend components increases monotonically with recovery time and does not attain a stationary value within our measurement time. For $t' < 50$ s the recovered stretch of the pure components is close to unity, which shows that the molecular recovery is very small. For $t' > 50$ s the recovered stretch increases because of the surface tension of the sample. This effect is more pronounced for the lower viscous SAN. The transient recovery of the blends differs significantly from $\lambda_r(t')$ of PA 6 and SAN. The recovered stretch of all blends rapidly increases for $t' < 20$ s. In this initial stage the PA30 blend attains the largest recovered stretch values, whereas the λ_r values of the PA50 and PA70 are similar. In Figure 4 the slope of the λ_r curve of the PA70 blend decreases considerably at $t' = 20$ s. A similar change of the slope is observed for the PA30 blend at $t' = 200$ s. On the contrary, the shape of the curve of the PA50 blend does not change much, and the λ_r values range between the λ_r values of PA70 and PA30 blends. At $t' = 42$ min the PA30 blend displays the largest recovered stretch with $\lambda_r = 5.2$, which is remarkably close to a fully reversible deformation $\lambda_r = \lambda_{max} = 6.0$. The λ_r value of the PA50 blend at $t' = 42$ min ranges between that of the PA30 and the PA70 blend ($\lambda_r = 3.2$ at $t' = 42$ min).

Morphological Investigations. In the micrographs the dark phase corresponds to SAN and the brighter phase to PA 6. The PA70 blend displays a droplet−matrix morphology (see Figure 5). The comparison of parts a and b of Figure 5 reveals that the morphology did not significantly change during sample preparation. The particle size distribution of the blend after sample preparation was obtained by measuring the radii r_i of the N circular cross sections of the drops. Drops with radius $r < 0.15$ μm are not included in the analysis because of the limited resolution. These small drops are most probably micelles and drops with a very high content of compatibilizer.[43,44] The number-average $\langle R_n \rangle$ and the volume average $\langle R_v \rangle$ of the true drop radius distribution follows from

$$\langle R_n \rangle = 4\langle r_n \rangle/\pi \tag{3}$$

$$\langle R_v \rangle = 32\langle r_s \rangle/(9\pi) \tag{4}$$

where $\langle r_n \rangle = (1/N)\sum_{i=1}^{N} r_i$ denotes the number-average and $\langle r_s \rangle = \sum_{i=1}^{N} r_i^3/\sum_{i=1}^{N} r_i^2$ the area average of the drop radius.[45−47] The number and the volume average of the particle radius are $\langle R_n \rangle = 0.42 \pm 0.01$ μm and $\langle R_v \rangle = 0.48 \pm 0.09$ μm.

In melt elongation the SAN domains of the PA70 blend are stretched into a highly extended shape which can be approximated by an ellipsoid of revolution (Figure 5c). In concentrated polymer blends, drops with different stretch ratios can collide and coalesce with a high probability.[35] In this blend coalescence is hindered (see the dashed circles in Figure 5c). Drops that are constrained in deformation by less elongated drops circumflow the less stretched drops which indicates that an interfacial layer at the surface of the drop prevents the

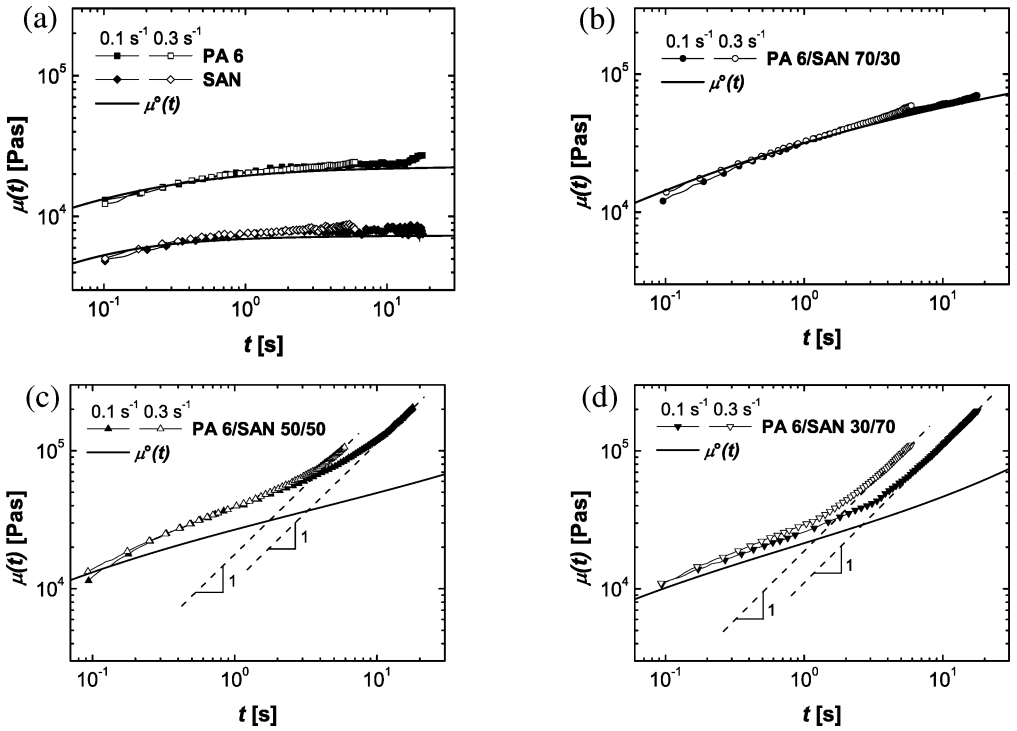

Figure 3. Elongational viscosity μ as a function of time t at $T = 240$ °C for (a) the blend components PA 6 and SAN, (b) the PA 6/SAN 70/30 blend, (c) the PA 6/SAN 50/50 blend, and (d) the PA 6/SAN 30/70 blend. The solid lines correspond to eq 13.

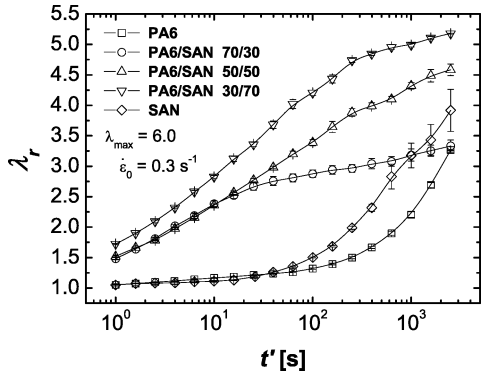

Figure 4. Recovered stretch λ_r as a function of recovery time t' for PA 6 and SAN and the three different PA 6/SAN blends at $T = 240$ °C. The maximum Hencky strain was $\epsilon_{max} = 1.8$, and the Hencky strain rate was $\dot{\epsilon}_0 = 0.3$ s^{-1}.

coalescence of drops. The stretch ratio λ_d of a drop is defined by the ratio of the major axis a of the ellipsoid to the initial particle diameter $2r_0$. Assuming that the drop is uniformly deformed such that λ_d is independent of the plane of cross section, the stretch ratio is given by

$$\lambda_d = (a'/b')^{2/3} \quad (5)$$

where a' denotes the major axis and b' the minor axis of the elliptical cross section of the ellipsoid. Figure 6 presents λ_d as a function of the equivalent radius $r_e = (a'b'^2)^{1/3}$. The stretch ratio λ_d increases with r_e. In order to examine the influence of reactive compatibilization on the deformation of the SAN drops, we compared the measured drop deformation with the theoretical prediction for uncompatibilized drops (see Figure 6). The average capillary number $Ca = \eta_m \dot{\epsilon}_0 \langle R_n \rangle / \alpha$ can be estimated by $Ca = 0.11$ with the interfacial tension $\alpha = 9.7$ mN/m, which was determined by the breaking thread method.[48] For $Ca \ll 1$ the stretch ratio of a drop with radius r_0 in a nondilute blend was calculated in ref 47 based on eqs 8 and 9 of ref 30 and the approach of Delaby[49] and is given by

$$\lambda_d(t = t_{max}) = \exp\{5F(p)Ca[1 - \exp(-t_{max}/\tau_1)]\} \quad (6)$$

with $p = \eta_d/\eta_m$, $F(p) = (19p + 16)/[40(p + 1) - 8\Phi(5p + 2)]$, $\tau_1 = \eta_m r_0[2p + 3 - 2\Phi(p - 1)](19p + 16)/\{4\alpha[10(p + 1) - 2\Phi(5p + 2)]\}$, $t_{max} = \epsilon_{max}/\dot{\epsilon}_0$, and the volume concentration Φ of the disperse phase. Figure 6 reveals that reactive compatibilization leads to a larger stretch ratio of the drops compared to the uncompatibilized case. This effect can be explained by a reduced interfacial tension α (see Figure 6) and by flow-induced convection of the compatibilizer to the drop tips which facilitates drop deformation compared to a uniform distribution of compatibilizer.[27] Since r_e is not the true drop radius r_0 and λ_d strongly depends on r_0 for small r_0 the λ_d values for $r_e < 0.4$ μm scatter very much. In addition, the scattering of λ_d may be also caused by different compatibilizer concentrations of the individual drops. However, larger deformed drops do not necessarily exhibit larger concentrations of compatibilizer. It was shown that high concentrations of compatibilizer can immobilize the interface and stabilize drops against deformation.[27,28]

At recovery time $t' = 42$ min the deformed drops have completely retracted back to a spherical shape (Figure 5d). The average drop radii after recovery were $\langle R_n \rangle = 0.38 \pm 0.01$ μm and $\langle R_v \rangle = 0.50 \pm 0.09$ μm. Obviously, they did not change much during elongation and recovery. This result confirms the qualitative observation of Figure 5c that coalescence is strongly suppressed in the PA70 blend. Figure 7 presents the morphology of the PA30 blend. PA 6 drops of roughly equal size are uniformly dispersed in the extruded strand (Figure 7a). After sample preparation the majority of the drops formed randomly shaped clusters (Figure 7b). In this case, compatibilization does not hinder the agglomeration of the drops in contrast to the PA70 blend but tremendously delays coalescence. Even after elongation and recovery of $t' = 42$ min the clusterlike character of the PA 6 domains persisted (Figure 7d).

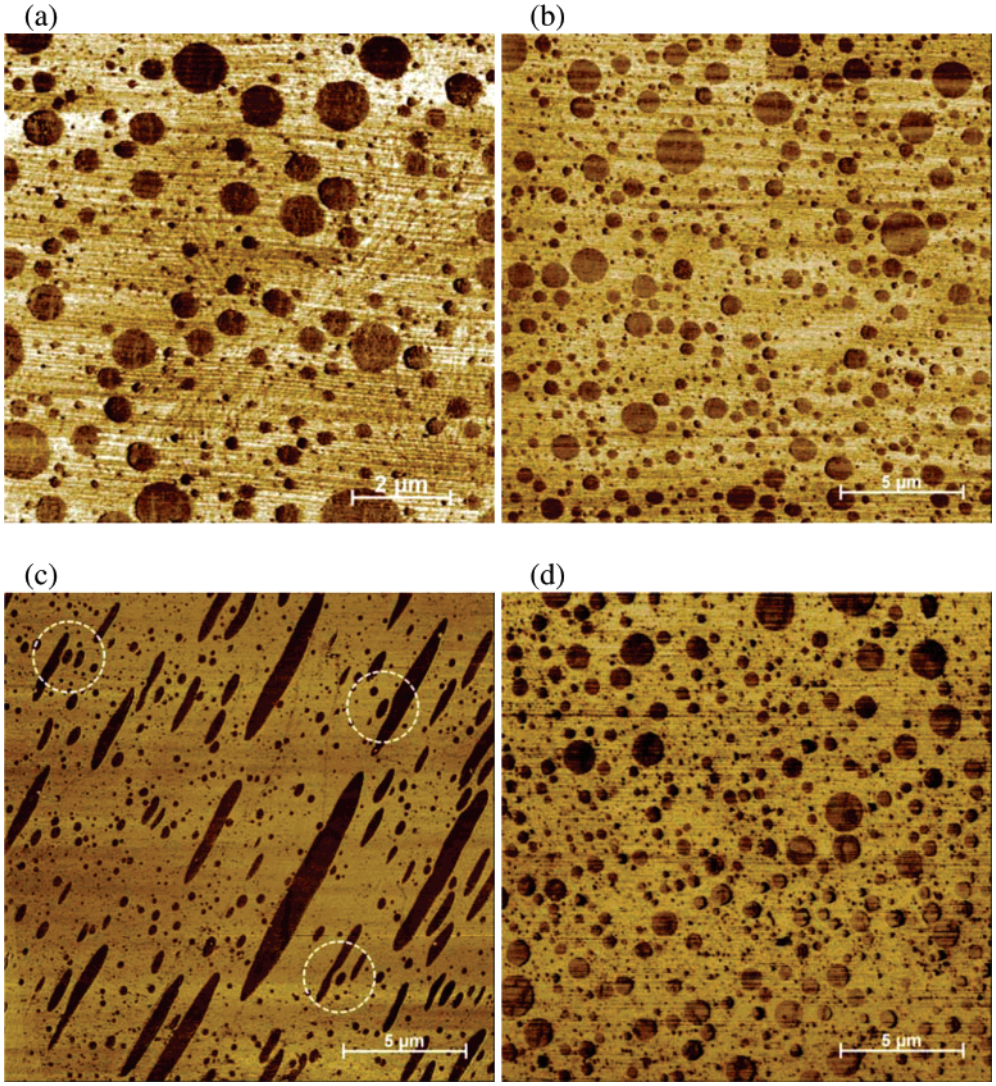

Figure 5. Atomic force micrographs of the PA 6/SAN 70/30 blend: (a) after extrusion, (b) after sample preparation, (c) elongated sample ($\epsilon_{max} = 1.8$, $\dot{\epsilon}_0 = 0.3\ s^{-1}$), and (d) recovered sample at recovery time $t' = 42$ min. Note the different scale bar in image (a).

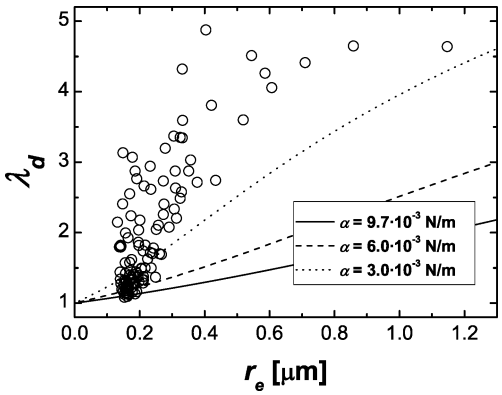

Figure 6. Stretch ratio λ_d of the drops as a function of the equivalent radius r_e; see eq 5 ($\epsilon_{max} = 1.8$, $\dot{\epsilon}_0 = 0.3\ s^{-1}$). The solid lines correspond to eq 6.

During elongation the PA 6 domains were oriented and strongly deformed. The deformation is not uniform, and for some domains necking occurs (Figure 7c). At recovery time t' = 42 min the morphology of the PA30 blend is very similar to its initial morphology without any preferential orientation of the phase domains (Figure 7d). The deformation of the PA 6 domains can be characterized by analyzing the 2d images. As a first approach, we use the maximum and the minimum Feret diameters F_{max} and F_{min}, which are defined by the maximum and minimum distance, respectively, between all possible parallel lines that are tangent to the cross-sectioned domain. The angle between the maximum (minimum) Feret diameter and the horizontal axis is denoted by the maximum (minimum) Feret angle ϕ_{max} (ϕ_{min}) (see Figure 8). The values of $\langle F_{max}\rangle$ and $\langle F_{min}\rangle$ slightly increased from 0.94 ± 0.08 μm and 0.58 ± 0.04 μm, respectively, before elongation to 1.15 ± 0.12 μm and 0.71 ± 0.07 μm at $t' = 42$ min, whereas the mean aspect ratio $\langle A_r\rangle = \langle F_{max}\rangle/\langle F_{min}\rangle$ was equal to 1.6 before elongation and at $t' =$ 42 min. In analogy to eq 5, we define the stretch ratio $\lambda_{\tilde{d}}$ of the PA 6 domains by

$$\lambda_{\tilde{d}} = (F_{max}/F_{min})^{2/3} \tag{7}$$

Figure 9 plots the probability density function $p_d(x)$ with $x = \lambda_{\tilde{d}} - 1$ for the initial, the elongated, and the recovered morphology and a fit of the log−normal distribution $p_{ln}(x) = 1/(\sqrt{2\pi}\sigma_{ln}x)\ \exp\{-[\ln(x/\kappa_{ln})]^2/(2\sigma_{ln}^2)\}$ with the parameters σ_{ln} and κ_{ln}. The values of $\lambda_{\tilde{d}}$ of the initial and the recovered morphology range between 1 and 2 with a maximum at ∼1.2 and 1.25, respectively. The elongated morphology depicts a large number of domains with $\lambda_{\tilde{d}} > 2$ with $|\phi_{max} - \phi_{min}| \approx \pi/2$ and attains its maximum at $\lambda_{\tilde{d}} \sim 1.6$.

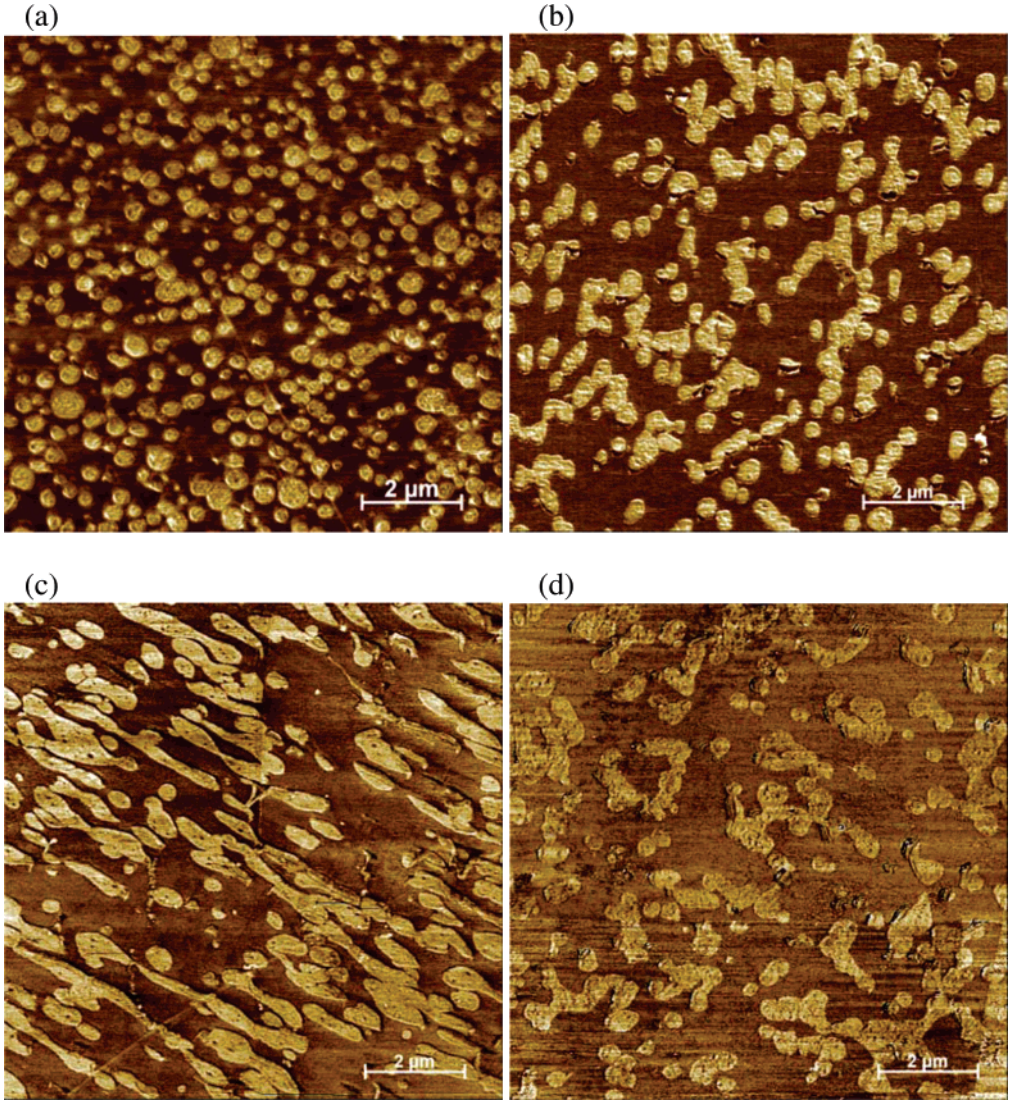

Figure 7. Atomic force micrographs of the PA 6/SAN 30/70 blend: (a) after extrusion, (b) after sample preparation, (c) elongated sample ($\epsilon_{max} = 1.8$, $\dot{\epsilon}_0 = 0.3\ s^{-1}$), and (d) recovered sample at recovery time $t' = 42$ min.

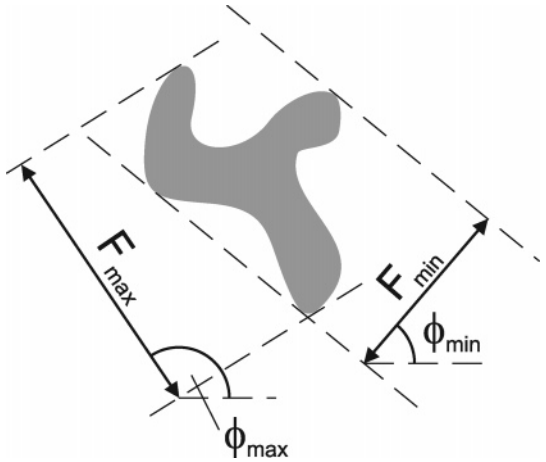

Figure 8. Definition of the maximum and minimum Feret diameters F_{max} and F_{min} and the maximum and minimum Feret angles ϕ_{max} and ϕ_{min}.

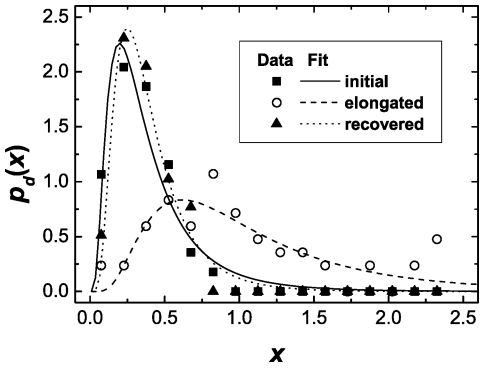

Figure 9. Probability density function $p_d(x)$ with $x = \lambda_{\tilde{d}} - 1$ of the PA 6 domains of the PA30 blend for the initial, the elongated ($\epsilon_{max} = 1.8$, $\dot{\epsilon}_0 = 0.3\ s^{-1}$), and the recovered morphology ($t' = 42$ min). A log−normal distribution function is fitted to the data.

The morphological processes during sample preparation of the PA50 blend are similar to the PA30 blend. Agglomeration and partial coalescence causes a change from a disperse morphology (Figure 10a) to a cocontinuous morphology during compression molding (Figure 10b). During elongation the cocontinuous phase domains were oriented and deformed (Figure 10c). After recovery ($t' = 42$ min), the morphology retracted to an isotropic shape (Figure 10d). In contrast to the PA30 blend the clusterlike character of the cocontinuous PA 6 domains of the undeformed sample (Figure 10b) has almost disappeared after elongation and recovery (Figure 10d). Similar to the other blends, SANMA micelles are located in the PA 6 domains.

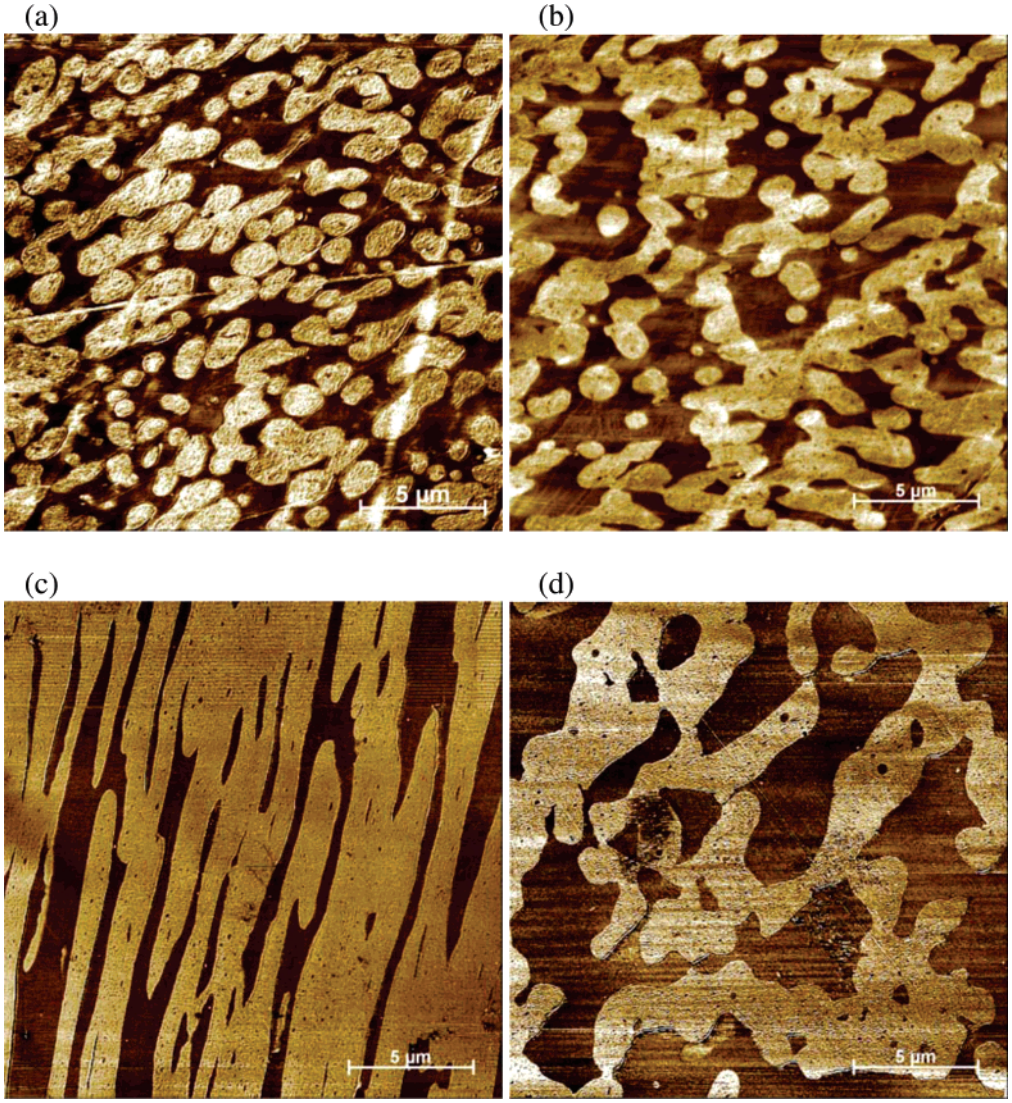

Figure 10. Atomic force micrographs of the PA 6/SAN 50/50 blend: (a) after extrusion, (b) after sample preparation, (c) elongated sample ($\epsilon_{max} = 1.8$, $\dot{\epsilon}_0 = 0.3\ s^{-1}$), and (d) recovered sample at recovery time $t' = 42$ min.

Discussion

Rheology. The complex modulus G^* of the reactively compatibilized blends strongly differs from G^* of the pure components. Particularly at low frequencies, G' and G'' of the blends do not satisfy the power laws $G' \propto \omega^2$ and $G'' \propto \omega$ which are typical for linear homopolymers and valid for a parallel arrangement of Maxwell models. In addition, the model of Palierne[13,14] cannot be fitted to the data of the blends with reasonable values of the interfacial tension α and the interfacial shear modulus β_{20}. Consequently, we apply an alternative linear viscoelastic approach for the phenomenological description of the data. This approach is associated with hierarchical arrangements of springs and dashpots, e.g., trees, ladders, or fractal structures.[50,51] Such hierarchical arrangements lead to rheological constitutive equations which involve fractional order time derivatives of the form

$$\sigma_{xy} = G_0 \tau_0^{\beta} \frac{d^{\beta}}{dt^{\beta}} \gamma \tag{8}$$

where σ_{xy} denotes the shear stress, γ the shear strain, τ_0 a characteristic time constant, G_0 the elastic modulus, and β the fractional exponent with $0 \le \beta \le 1$. The mathematical formalism of fractional calculus is described in refs 50−54.

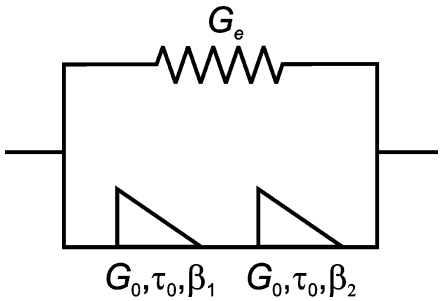

Figure 11. The Zener model with fractional elements (depicted by triangles).

Equation 8 represents the constitutive equation of a single fractional element and describes generalized viscoelastic behavior ranging from linear elastic ($\beta = 0$) to purely viscous behavior ($\beta = 1$).

In this study, we applied a fractional generalization of the Zener model which consists of two fractional elements in series and a spring in parallel (see Figure 11). The constitutive equation of the model is[52,54]

$$\sigma_{xy} + \tau_0^{\alpha} \frac{d^{\alpha}}{dt^{\alpha}} \sigma_{xy} = G_e \left(\gamma + \tau_0^{\alpha} \frac{d^{\alpha}}{dt^{\alpha}} \gamma \right) + G_0 \tau_0^{\beta} \frac{d^{\beta}}{dt^{\beta}} \gamma \tag{9}$$

Table 3. Fit Parameters of the Fractional Zener Model[a]

blend	β_1	β_2	τ_0 (s)	G_0 (10^4 Pa)	G_e (Pa)
PA 6	1.0	0.46	9.76×10^{-2}	7.80	0
PA 6/SAN 70/30	0.85	0.45	2.89×10^{-1}	4.27	0
PA 6/SAN 50/50	0.77	0.25	1.50×10^{-2}	2.21	57
PA 6/SAN 30/70	0.72	0.16	5.88×10^{-3}	2.83	262
SAN	1.0	0.34	4.93×10^{-2}	4.96	0

[a] The SAN grade includes 6.8 wt % SANMA.

with $\alpha = \beta_1 - \beta_2 > 0$ and $\beta = \beta_1$. Here β_1 and β_2 denote the fractional exponents, τ_0 a characteristic time, and G_0 the modulus of the fractional elements. The elastic modulus of the spring is denoted by G_e. The complex modulus $G^* = G' + iG''$ follows from a Laplace transformation of eq 9:[55]

$$G^*(\omega) = G_e + G_0 \frac{(i\omega\tau_0)^\beta}{1 + (i\omega\tau_0)^\alpha} \tag{10}$$

The real and the imaginary part of G^* are given by

$$G'(y) = G_e + G_0 y^\beta \frac{\cos(\beta\pi/2) + y^\alpha \cos[(\beta - \alpha)\pi/2]}{1 + 2y^\alpha \cos(\alpha\pi/2) + y^{2\alpha}} \tag{11}$$

$$G''(y) = G_0 y^\beta \frac{\sin(\beta\pi/2) + y^\alpha \sin[(\beta - \alpha)\pi/2]}{1 + 2y^\alpha \cos(\alpha\pi/2) + y^{2\alpha}} \tag{12}$$

with $y = \omega\tau_0$.

In contrast to the generalized Maxwell model, the fractional Zener model includes only five parameters, i.e., β_1, β_2, τ_0, G_0, and G_e. Applying a nonlinear least-squares fit and taking into account the condition $\beta_1 \leq 1$, eqs 11 and 12 were fitted to the experimental data (see Table 3). The good agreement between the model and the data demonstrates the applicability of the model (see Figure 2). The low-frequency behavior of the blend components is described by the fractional exponent $\beta_1 = 1$ and a zero elastic modulus G_e. In the case of the reactively compatibilized blends β_1 is smaller than one, and for PA50 and PA30 the elastic modulus is nonzero. The terminal behavior is given by $G' = G_e$, $G'' \propto \omega^{\beta_1}$ for PA50 and PA30, and $G' \propto \omega^{\beta_1}$, $G'' \propto \omega^{\beta_1}$ for PA70. The values of β_1 and β_2 and the characteristic time constant τ_0 decrease with increasing content of SAN.

Reactive compatibilization strongly influences the linear viscoelastic properties of the blends. The increase of G' and G'' of the PA70 blend cannot be explained by the model of Palierne.[13,14] In our case additional relaxation processes exist which are associated with the multigrafted SANMA chains. In addition, the PA50 and the PA30 blend display a nonzero equilibrium modulus G_e which is commonly explained by a networklike structure. Taking into account that surface grafting of particles favors particle−particle interactions and causes a low-frequency plateau modulus,[56,57] we explain the solidlike low-frequency behavior of the PA30 blend by elastic interactions between the grafted shells of the compatibilized PA 6 domains.

The transient elongational viscosity $\mu(t)$ of the reactively compatibilized blends does not obey a mixing rule for the viscosity of the blend components in contrast to uncompatibilized blends.[36,37] In order to check whether the linear viscoelastic prediction of the transient elongational viscosity $\mu^\circ(t) = 3\eta^\circ(t)$ agrees with the measured values of the elongational viscosity $\mu(t)$, the transient linear shear viscosity $\eta^\circ(t) = \int_0^t G(t')\,dt'$ was calculated, where $G(t)$ denotes the transient shear modulus of the fractional Zener model:[52]

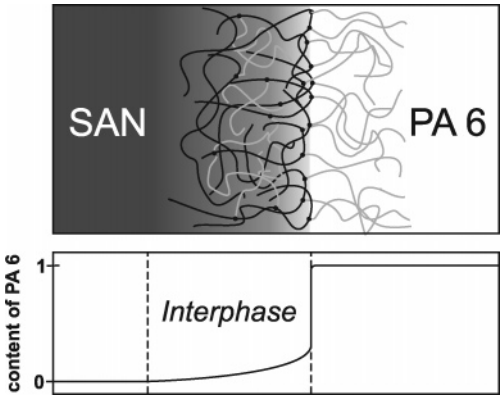

Figure 12. Schematic illustration of the interface of reactively compatibilized PA 6/SAN blends.

$$\eta^\circ(t) = G_e t + G_0 \int_0^t (t'/\tau_0)^{-\beta} E_{\alpha,1-\beta}[-(t'/\tau_0)^\alpha]\,dt' \tag{13}$$

with the generalized Mittag−Leffler function $E_{\kappa,\nu}[x] = \sum_{n=0}^{\infty} x^n/[\Gamma(n\kappa + \nu)]$ and the Gamma function $\Gamma(x)$. The agreement between $\mu(t)$ and $\mu^\circ(t)$ is good for the blend components and the PA70 blend (Figure 2a,b). The small mismatch for PA 6 at large t is caused by the exponentially decreasing cross section of the sample and the force resolution. In the case of the PA50 blend and the PA30 blend $\mu(t)$ exceeds the linear viscoelastic prediction (Figure 2c,d). The discrepancy between $\mu(t)$ and $\mu^\circ(t)$ increases with time and strain, respectively. The dashed lines of slope of unity in Figure 3c,d indicate $\mu \propto t$ and $\sigma \propto \epsilon$, respectively. This solidlike strain rate dependent stress−strain relation of the blends at larger strains possibly originates from the transient network that causes the low-frequency plateau of G'. The solidlike behavior is mostly pronounced for the PA30 blend.

The transient recovered stretch of the blends in Figure 4 results from the molecular recovery of the blend components, the interfacial tension driven recovery, and the effect of reactive compatibilization. Since the molecular recovery of the pure components is very small, the different transient recovery of the blends is caused by the different morphologies and by the effects of reactive compatibilization. The elastic response of the transient network between the PA 6 domains contributes to the recovered stretch of the PA30 blend and leads to the remarkably high value compared to the PA70 blend. In the latter case the morphology mainly contributes to the recovered stretch. Analogous to the linear viscoelastic properties and the transient behavior in elongation the PA50 blend shows intermediate behavior.

Coalescence and Deformation of Domains. Ideally, the compatibilizer is located at the interface such that the SANMA backbone is located in the SAN domain and the grafted PA 6 chains expand into the PA 6 domain. The molecular weight of the grafted PA 6 is identical with the molecular weight of the bulk (M_w = 121 000 g/mol) and strongly exceeds the critical molecular weight M_c for entanglement coupling of PA 6, $M_c \approx$ 5000 g/mol.[58] In ref 40 it was shown that a complete conversion of maleic anhydride can be experimentally assumed. Then the average molecular weight of the segments of the SANMA backbone between neighboring grafting points M_s is estimated by $M_s \approx M_w/20 \approx$ 5800 g/mol. This value is considerably smaller than the critical molecular weight of SAN $M_c \approx$ 22 000 g/mol.[59] Therefore, the bulk SAN does not entangle with the loops of the SANMA and is repelled from the interface. This

asymmetric situation is related to the wet and dry brush conditions of Leibler's theory[60] and leads for asymmetric diblock copolymer to the bending of the interface toward the shorter block.[61] In this case the asymmetry of the compatibilizer causes the bending of the interface toward the SAN domain and favors the formation of micelles with a SANMA-rich core in all blends.[62] Furthermore, the assumption that all grafted PA 6 chains are located in the PA 6 domain represents a strong constraint for the conformation of multigrafted SANMA chains. Single-grafted PA 6 may be expelled from the interface and trapped in the SAN domain close to the interface. In that way an interphase of grafted SANMA with a nonzero concentration of PA 6 is formed (see Figure 12). On the basis of extraction experiments and measurements of the interfacial thickness, qualitatively similar pictures of reactively compatibilized interfaces were proposed.[63,64] The different chemical composition of the interphase compared to the bulk SAN favors aggregation of the PA 6 drops of the PA30 blend. Because of the high degree of compatibilization, further coalescence is efficiently decreased such that the clusterlike character of the domains is retained even after elongation and recovery (Figure 7d). Interactions between the interphases of neighboring PA 6 domains lead to the formation of an elastic network which causes solidlike behavior at low frequencies and strain hardening in elongation. The network persisted high elongations and increased the recoverable strain of the blend. In the case of the PA70 blend the grafted PA 6 chains that are identical to the bulk PA 6 form a layer on the surface of the SAN droplets which stabilizes the drops against agglomeration and coalescence.

Conclusions

Reactive compatibilization through maleic anhydride-functionalized SAN strongly influences the viscosity, the elasticity, and the morphology of PA 6/SAN blends in the melt. Depending on the composition ratio and compatibilizer concentration of the blends different morphological and rheological phenomena were observed in this study. We explain these observations by the asymmetric nature of the reactively compatibilized interface. On the one hand, reactive compatibilization generates an interfacial layer of grafted PA 6 chains at the surface of the SAN domains which inhibits coalescence. On the other hand, reactive compatibilization causes the formation of an interphase consisting of PA 6 grafted terpolymer chains on the surface of the PA 6 domains. The specific chemical composition of the interphases favors agglomeration of the PA 6 drops and interactions between the interphases of neighboring particles which causes a solidlike low-frequency behavior. In elongation this transient network leads to strain hardening with a linear relation between stress and Hencky strain. During recovery the elastic response of the network and the interfacial tension driven recovery of the deformed phase domains superpose and lead to a larger recovered stretch of the PA30 blend compared to the PA70 blend. In a future investigation we will vary the compatibilizer concentration of the PA70 blend and PA30 blend in order to study the influence of compatibilizer concentration.

Acknowledgment. The authors are indebted to Dr. M. Weber and Dr. H. Steininger (BASF AG, Ludwigshafen am Rhein, Germany) for very helpful discussions and for supplying the materials of this study. The valuable discussions with Professors J. Meissner and H. C. Öttinger are also gratefully acknowledged. The authors thank W. Schmidheiny, F. Mettler, and J. Hostettler for their continuous support of the experiments and M. Colussi for the DSC and GPC measurements. They are also thankful to the Swiss National Science Foundation for financial support (Project No. 200021-103287).

References and Notes

(1) Utracki, L. A. *Polymer Alloys and Blends*, 2nd ed.; Hanser: Munich, 1989.
(2) Paul, D. R.; Bucknall, C. B. *Polymer Blends*, 2nd ed.; Wiley: New York, 2000; Vols. 1 and 2.
(3) Ajji, A.; Utracki, L. A. *Polym. Eng. Sci.* **1996**, *36*, 1574−1585.
(4) Koning, C.; van Duin, M.; Pagnoulle, C.; Jerome, R. *Prog. Polym. Sci.* **1998**, *23*, 707−757.
(5) Macosko, C. W.; Jeon, H. K.; Hoye, T. R. *Prog. Polym. Sci.* **2005**, *30*, 939−947.
(6) Triacca, V. J.; Ziaee, S.; Barlow, J. W.; Keskkula, H.; Paul, D. R. *Polymer* **1991**, *32*, 1401−1413.
(7) Takeda, Y.; Paul, D. R. *J. Polym. Sci., Part B: Polym. Phys.* **1992**, *30*, 1273−1284.
(8) Majumdar, B.; Keskkula, H.; Paul, D. R. *Polymer* **1994**, *35*, 3164−3172.
(9) Majumdar, B.; Keskkula, H.; Paul, D. R.; Harvey, N. G. *Polymer* **1994**, *35*, 4263−4279.
(10) Jeon, H. K.; Kim, J. K. *Macromolecules* **1998**, *31*, 9273−9280.
(11) Kudva, R. A.; Keskkula, H.; Paul, D. R. *Polymer* **2000**, *41*, 239−258.
(12) Jafari, S. H.; Pötschke, P.; Stephan, M.; Warth, H.; Alberts, H. *Polymer* **2002**, *43*, 6985−6992.
(13) Palierne, J. F. *Rheol. Acta* **1990**, *29*, 204−214.
(14) Palierne, J. F. *Rheol. Acta* **1991**, *30*, 497−497.
(15) Asthana, H.; Jayaraman, K. *Macromolecules* **1999**, *32*, 3412−3419.
(16) Riemann, R. E.; Cantow, H. J.; Friedrich, C. *Macromolecules* **1997**, *30*, 5476−5484.
(17) Moan, M.; Huitric, J.; Mederic, P.; Jarrin, J. *J. Rheol.* **2000**, *44*, 1227−1245.
(18) Van Hemelrijck, E.; Van Puyvelde, P.; Velankar, S.; Macosko, C. W.; Moldenaers, P. *J. Rheol.* **2004**, *48*, 143−158.
(19) Van Hemelrijck, E.; Van Puyvelde, P.; Macosko, C. W.; Moldenaers, P. *J. Rheol.* **2005**, *49*, 783−798.
(20) Wang, J.; Velankar, S. *Rheol. Acta* **2006**, *45*, 297−304.
(21) Wang, J.; Velankar, S. *Rheol. Acta* **2006**, *45*, 741−753.
(22) Van Puyvelde, P.; Velankar, S.; Moldenaers, P. *Curr. Opin. Colloid Interface Sci.* **2001**, *6*, 457−463.
(23) Jeon, H. K.; Macosko, C. W. *Polymer* **2003**, *44*, 5381−5386.
(24) Stone, H. A.; Leal, L. G. *J. Fluid Mech.* **1990**, *220*, 161−186.
(25) Milliken, W. J.; Stone, H. A.; Leal, L. G. *Phys. Fluids A* **1993**, *5*, 69−79.
(26) Pawar, Y.; Stebe, K. J. *Phys. Fluids* **1996**, *8*, 1738−1751.
(27) Hu, Y. T.; Pine, D. J.; Leal, L. G. *Phys. Fluids* **2000**, *12*, 484−489.
(28) Van Puyvelde, P.; Velankar, S.; Mewis, J.; Moldenaers, P. *Polym. Eng. Sci.* **2002**, *42*, 1956−1964.
(29) Gramespacher, H.; Meissner, J. *J. Rheol.* **1992**, *36*, 1127−1141.
(30) Graebling, D.; Muller, R.; Palierne, J. F. *Macromolecules* **1993**, *26*, 320−329.
(31) Vinckier, I.; Moldenaers, P.; Mewis, J. *J. Rheol.* **1996**, *40*, 613−631.
(32) Vinckier, I.; Laun, H. M. *J. Rheol.* **2001**, *45*, 1373−1385.
(33) Steinmann, S.; Gronski, W.; Friedrich, C. *Rheol. Acta* **2002**, *41*, 77−86.
(34) Mechbal, N.; Bousmina, M. *Rheol. Acta* **2004**, *43*, 119−126.
(35) Heindl, M.; Sommer, M. K.; Münstedt, H. *Rheol. Acta* **2004**, *44*, 55−70.
(36) Handge, U. A.; Pötschke, P. *J. Rheol.* **2004**, *48*, 1103−1122.
(37) Handge, U. A.; Pötschke, R. *J. Rheol.* **2005**, *49*, 1553−1553.
(38) Majumdar, B.; Paul, D. R.; Oshinski, A. J. *Polymer* **1997**, *38*, 1787−1808.
(39) van Duin, M.; Machado, A. V.; Covas, J. *Macromol. Symp.* **2001**, *170*, 29−39.
(40) Weber, M.; Heckmann, W.; Goeldel, A. *Macromol. Symp.* **2006**, *233*, 1−10.
(41) Meissner, J.; Hostettler, J. *Rheol. Acta* **1994**, *33*, 1−21.
(42) Handge, U. A.; Schmidheiny, W. *Rheol. Acta*, in press.
(43) Charoensirisomboon, P.; Inoue, T.; Weber, M. *Polymer* **2000**, *41*, 6907−6912.
(44) Jeon, H. K.; Zhang, J. B.; Macosko, C. W. *Polymer* **2005**, *46*, 12422−12429.
(45) Goldsmith, P. L. *Br. J. Appl. Phys.* **1967**, *18*, 813−830.
(46) Okamoto, K.; Takahashi, M.; Yamane, H.; Kashihara, H.; Watanabe, H.; Masuda, T. *J. Rheol.* **1999**, *43*, 951−965.
(47) Handge, U. A.; Okamoto, K.; Münstedt, H., submitted for publication.
(48) Elemans, P. H. M.; Janssen, J. M. H.; Meijer, H. E. H. *J. Rheol.* **1990**, *34*, 1311−1325.
(49) Delaby, I.; Ernst, B.; Muller, R. *Rheol. Acta* **1995**, *34*, 525−533.
(50) Schiessel, H.; Blumen, A. *J. Phys. A: Math. Gen.* **1993**, *26*, 5057−5069.

(51) Heymans, N.; Bauwens, J. C. *Rheol. Acta* **1994**, *33*, 210−219.
(52) Schiessel, H.; Metzler, R.; Blumen, A.; Nonnenmacher, T. F. *J. Phys. A: Math. Gen.* **1995**, *28*, 6567−6584.
(53) Schiessel, H.; Blumen, A. *Macromolecules* **1995**, *28*, 4013−4019.
(54) Heymans, N. *Rheol. Acta* **1996**, *35*, 508−519.
(55) Friedrich, C. *J. Non-Newtonian Fluid Mech.* **1993**, *46*, 307−314.
(56) Aoki, Y. *Macromolecules* **1987**, *20*, 2208−2213.
(57) Fahrländer, M.; Bruch, M.; Menke, T.; Friedrich, C. *Rheol. Acta* **2001**, *40*, 1−9.
(58) van Krevelen, D. W. *Properties of Polymers*, 3rd ed.; Elsevier: Amsterdam, 1990.
(59) Wu, S. H. *Polymer* **1987**, *28*, 1144−1148.
(60) Leibler, L. *Makromol. Chem., Macromol. Symp.* **1988**, *16*, 1−17.
(61) Mezzenga, R.; Fredrickson, G. H.; Kramer, E. J. *Macromolecules* **2003**, *36*, 4457−4465.
(62) Kitayama, N.; Keskkula, H.; Paul, D. R. *Polymer* **2000**, *41*, 8053−8060.
(63) Dedecker, K.; Groeninckx, G. *Macromolecules* **1999**, *32*, 2472−2479.
(64) Yukioka, S.; Inoue, T. *Polymer* **1994**, *35*, 1182−1186.

MA062705C